Advancements in the Mechanical Structure Design of FalconD: The INFN-CERN Collaboration for the Nb_3Sn 12 T Cos-Theta Dipole Within the High-Field Magnets R&D Program

T. Maiello, A. Bersani, E. Bianchi, B. Caiffi, A. Dellacasagrande, S. Farinon, A. Foussat, A. Gagno, L. Musenich, A. Pampaloni, N. Sala, M. Sorbi, E. Todesco, and R. U. Valente

***Abstract*—The FalconD project (Future Accelerator post-LHC Optimized Nb_3Sn Dipole), conducted by INFN Genoa and Milan in collaboration with CERN, is dedicated to the development of a 1.5 m long, 12 T Nb_3Sn dipole. Nb_3Sn has already proven its effectiveness in accelerator magnets, and its application to bending dipoles is a key step toward future high-field accelerator technologies. A major challenge of the design is the mechanical structure, which must withstand the substantial Lorentz forces generated by the high magnetic field. To address this, the innovative bladder and key (B & K) concept is adopted, applied here for the first time to a cos-theta dipole. This contribution presents a 2D finite element mechanical analysis of the FalconD, focusing on stress distribution and gap evolution during the main assembly and operational stages, with the aim of validating the design approach.**

***Index Terms*—Accelerator dipoles, superconducting magnets, Nb_3Sn, mechanical systems.**

I. Introduction

THE realization of next-generation particle accelerators, including the proposed Future Circular Collider [1], depends on significant advances in magnet technology, with particular emphasis on high-field bending dipoles. These magnets play a central role in guiding and focusing particle beams, thereby ensuring both accurate control and efficient machine operation. As accelerator designs aim for higher energies and luminosities, the demand grows for dipoles capable of sustaining stronger fields without compromising stability or reliability. Meeting these requirements is closely tied to the choice of superconducting materials. Among available options, Nb_3Sn has established itself as the most promising material for high-field applications [2]. Compared with NbTi, it exhibits superior performance, above 10 T. Its capabilities have already been proven in the MQXF quadrupoles [3], developed for the High-Luminosity LHC upgrade, where the use of Nb_3Sn enables higher magnetic fields and more compact magnet layouts. Building on this success, research efforts are increasingly directed toward Nb_3Sn dipole magnets, which are essential for future circular colliders and other advanced accelerator infrastructures. The FalconD (Future Accelerator post-LHC Cos-theta Optimised Nb_3Sn Dipole) project, carried out jointly by CERN and the INFN divisions of Genoa and Milan, aims to design and build a 12 T cos-theta dipole [4], [5], [6], [7], [8], [9], [10], [11]. The project is conceived to explore the performance boundaries of Nb_3Sn while addressing the technological challenges associated with magnet design, coil fabrication, and material behavior. As a prototype, the FalconD dipole is intended to pave the way for the magnets of future high-energy physics facilities beyond the LHC. A core component of the project is the construction of high-performance superconducting coils, a task entrusted to ASG Superconductors, a company with extensive expertise in superconducting magnet manufacturing. Achieving success requires overcoming demanding technical issues, such as refining coil geometry, mitigating electromagnetic stresses, and ensuring reliable operation at high fields. This paper presents the FalconD project, offering a comprehensive overview of the magnet's characteristics, from its geometric configuration to its material properties. Particular attention is devoted to the mechanical aspects and design strategy of the 12 T dipole, with a detailed FEM analysis leading to the results.

Received 13 October 2025; revised 12 December 2025; accepted 29 December 2025. Date of publication 15 January 2026; date of current version 26 January 2026. This work was supported by HFM Program. *(Corresponding author: T. Maiello.)*

T. Maiello, A. Bersani, E. Bianchi, B. Caiffi, S. Farinon, and A. Gagno are with the Istituto Nazionale di Fisica Nucleare Sezione di Genova, 16146 Genova, Italy (e-mail: tommaso.maiello@ge.infn.it).

A. Dellacasagrande is with the Istituto Nazionale di Fisica Nucleare Sezione di Genova, 16146 Genova, Italy, and also with the Università degli Studi di Genova, 16126 Genova, Italy.

A. Foussat, N. Sala, and E. Todesco are with the European Organization for Nuclear Research, 1211 Geneva, Switzerland.

L. Musenich is with the Università degli Studi di Genova, 16126 Genova, Italy.

A. Pampaloni is with the Istituto Nazionale di Fisica Nucleare Sezione di Genova, 16146 Genova, Italy, and also with the Università degli Studi di Roma "La Sapienza," 00185 Roma, Italy.

M. Sorbi is with the Istituto Nazionale di Fisica Nucleare, Laboratorio Acceleratori e Superconduttività Applicata, 20090 Milano, Italy, and also with the Università degli Studi di Milano, 20122 Milano, Italy.

R. U. Valente is with the Istituto Nazionale di Fisica Nucleare, Laboratorio Acceleratori e Superconduttività Applicata, 20090 Milano, Italy.

Color versions of one or more figures in this article are available at https://doi.org/10.1109/TASC.2026.3652970.

Digital Object Identifier 10.1109/TASC.2026.3652970

II. FalconD Main Properties

The magnet is a short model, 1.5 m in length, featuring a single 50 mm aperture and composed of two-layer coils in a cos-θ configuration, as illustrated in Fig. 1. To ensure the coil stress remains below 120 MPa (yield strength of the conductors)

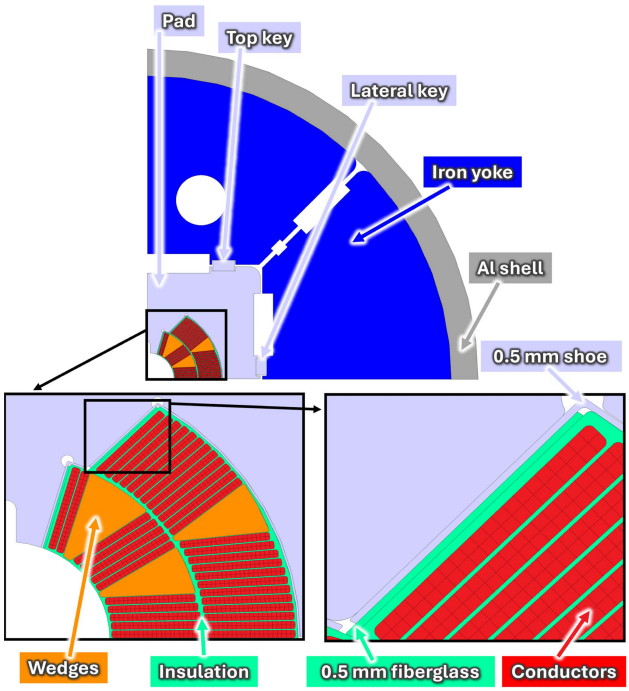

Fig. 1. Cross-section of FalconD.

TABLE I
GEOMETRIC AND MAGNETIC FEATURES OF FALCOND

Parameter	Value
No. of strands in a cable	40
Reacted bare cable width	21.42 mm
Reacted bare cable thin edge	1.797 mm
Reacted bare cable thick edge	1.989 mm
Aperture diameter	50 mm
Nominal current	21677 A
Engineering current density	483 A/mm^2
Bore magnetic field	12 T
Peak field in conductors	12.51 T
Physical length	1.5 m
Operating temperature	1.9 K
Margin on loadline @ 1.9 K	23 %

and to avoid irreversible degradation of the Nb_3Sn material, a bladder-and-key system [12] is used. The conductor employed is a high-performance Nb_3Sn RRP round wire, 1 mm in diameter, with a critical current density of 1200 A/mm^2 at 4.2 K and 16 T [2]. The coils are wound using a Rutherford cable composed of 40 strands, with dimensions of 21.42 mm in width and 1.89 mm in thickness (average value), accounting for expansion during the heat-treatment process. The coil winding presents significant challenges due to the narrow bending radii imposed by the cable width, resulting in a five-block configuration per quadrant. Field quality is not the main priority, as the design prioritizes a balance between performance and manufacturability. The magnet generates a bore field of 12 T at an operating current of approximately 22 kA (about 500 A/mm^2), with a peak-field inside the cable of 12.51 T. The operating margin of the peak field load line is 23% at 1.9 K and 15% at 4.2 K. All these values are summarized in the Table I

Regarding the other components of the magnet, 0.5 mm thick fiberglass layers are attached to the coils at the pole in order to provide the cables with better insulation from the rest of the magnet. In addition, 0.5 mm thick stainless-steel (SS) shoe

TABLE II
MATERIAL PROPERTIES AT ROOM TEMPERATURE AND CRYOGENIC TEMPERATURE (293 K, 1.9 K)

	Conductors	Fiberglass[1]
E_{rad} [GPa]	53, 58	15.51, 20
E_θ [GPa]	38, 43	8.29, 12.5
ν_{xy}	0.25, 0.25	0.301, 0.21
α_{rad} [mm/m]	3.88 10^{-3}	2.46 10^{-3}
α_θ [mm/m]	3.88 10^{-3}	7.17 10^{-3}
σ_y [MPa]	100, 120	150, 150

	Cu Wedges	SS316LN	Iron ARMCO	Al 7075
E [GPa]	110, 110	193, 210	213, 224	70, 79
ν_{xy}	0.3, 0.3	0.28, 0.28	0.3, 0.3	0.33, 0.33
α [mm/m]	3.1 10^{-3}	2.95 10^{-3}	2.0 10^{-3}	4.2 10^{-3}
σ_y [MPa]	270, 340	238, 610	210, 720	480, 490
R_m [MPa]	350, 540	565, 1455	286, 975	–, 650

surrounds the conductors, providing mechanical protection from the SS pad in all directions, not only on the pole. This configuration helps to mediate the mechanical containment exerted by the pad, improving stress distribution and reducing stress peaks within the conductor. The SS pad is square, with sides of 105 mm, while the keys measure 20 mm in width for the top key, featuring an interference of 0.2 mm, and 15 mm for the lateral key, with an interference of 0.1 mm. The bladders designed for this magnet are 56 mm wide. Along the diagonals of the cross section (see Fig. 1), there are dedicated slots for bladder and keys that help maintain the yokes in their correct position during assembly. However, this aspect has not yet been investigated in detail. Finally, the iron yoke has an outer radius of 283 mm, while the aluminum outer shell has a thickness of 25 mm. All these details are illustrated clearly in Fig. 1.

III. 2D MECHANICAL MODEL

The 2D mechanical model of the dipole is complete and now enters the engineering phase, where structural details are refined to ensure reliable performance. Using Ansys Mechanical APDL (version 2022 R2), a four-step finite element analysis was conducted to investigate the magnet's mechanical behavior throughout its various operational phases. In the first step, the vertical and horizontal bladders were pressurized to 30 MPa to verify that the magnet could be sufficiently opened for key insertion. The subsequent analysis steps include key insertion (activation of contacts), cooling to 1.9 K, and magnet energization with Lorentz forces. Only one quarter of the cross section was modeled, applying the appropriate symmetry constraints to accurately reproduce the system's behavior (the x and y axes coincide with the axes of symmetry). For the mechanical analysis, the 2D element used has four sides, eight nodes and quadratic displacement. Instead the contact friction coefficient is 0.2 in all the contacts. All materials are treated as linearly elastic. Table II summarizes their main properties: Young's modulus (E), Poisson's ratio (ν), thermal expansion coefficient (α), yield strength (σ_y) and ultimate strength (R_m), expressed in either Cartesian (x–y) or polar (rad–θ) coordinates. Isotropic values, and behavior, are assumed when unspecified. Material properties, except for conductors, are based on the article by Vallone et al. [13]. Regarding conductors, specific studies and stack tests are currently being carried out at CERN [14].

[1]The plane of the fibers is xz (radial-axial).

TABLE III
LORENTZ FORCE COMPONENTS AND KEY INTERFERENCES

Layer	Component	Value [MN/m]
First	F_X	+2.26
First	F_Y	-0.33
Second	F_X	+1.25
Second	F_Y	-1.59
Top key	Interference	0.2 mm
Lateral key	Interference	0.1 mm

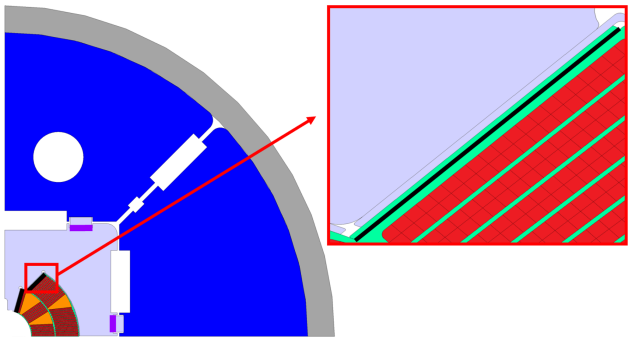

Fig. 2. Types of contacts in the mechanical model: sliding (purple lines), glued (black lines), and sliding/detachable (other interfaces).

TABLE IV
RELATIVE DISPLACEMENTS OF THE MEASURED POINT PAIRS

Point Pair	$\lvert\Delta X\rvert$ [mm]	Point Pair	$\lvert\Delta Y\rvert$ [mm]
A1-A2	0.41	D1-D2	0.52
B1-B2	0.41	E1-E2	0.51
C1-C2	0.41	F1-F2	0.50

The magnet relies on a bladder-and-key support system [12]. As shown in Fig. 1, SS shoes and laminated pads enclose the coils, providing support, stress reduction, and alignment. These are surrounded by a laminated yoke (four 90° sectors) and an aluminum outer shell that enhances structural strength. The bladder & key system and the shell apply coil preload in two stages: first during assembly at room temperature (bladder pressurization and key insertion), then during cooldown, exploiting the higher thermal contraction of aluminum. This approach ensures effective containment of Lorentz forces while protecting the brittle Nb_3Sn conductors. Table III shows the Lorentz forces and the corresponding key interferences.

These forces constitute the dominant mechanical loads that the structure must resist in order to preserve the magnet's stability and structural integrity.

IV. ANSYS RESULTS

First of all, contact management was implemented as follows: sliding contacts (keys-pad, purple lines), glued contacts (fiberglass-insulation, black lines), and sliding/detachable contacts (all remaining interfaces). A visual clarification is provided in Fig. 2.

Regarding to the first step, three pairs of reference points were defined at each key location (on the SS pad and the corresponding iron surface, see Fig. 3), and their relative displacements were compared with the required interference. The results are reported in Table IV.

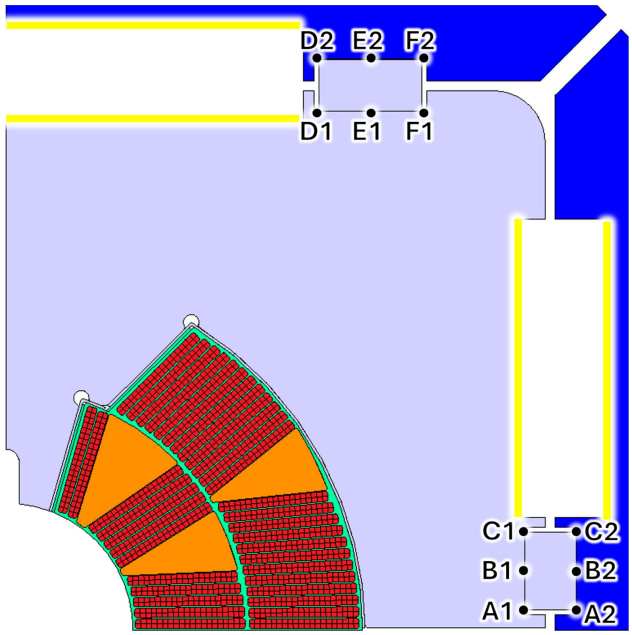

Fig. 3. Pairs of points used to study the opening of the gaps where the keys will be inserted. Yellow lines mark the regions where a pressure of 30 MPa is applied, simulating bladder inflation.

TABLE V
PEAK STRESSES AND CORRESPONDING LIMITS IN ALL MATERIALS AT RT AND 1.9 K

	VM_{peak} [MPa]	σ_y [MPa]	R_m [MPa]
Conductors	89, 118	100, 120	–, –
Wedges	84, 130	270, 340	350, 540
Shoe	422, 888	238, 610	565, 1455
Pad	292, 684	238, 610	565, 1455
Keys	104, 594	238, 610	565, 1455
Yoke	81, 308	210, 720	286, 975
Shell	132, 163	480, 490	–, 650

As shown in Table IV, the gap is sufficient for key insertion, with margin for possible misalignments (an overshoot of 0.2 mm). Regarding to the other steps, Table V summarizes the Von Mises (VM) peak stresses of the different materials at RT and 1.9 K, compared with their mechanical limits.

The results show that all values remain below the allowable mechanical limits and are therefore acceptable. In the specific case of the SS shoe and pad, the peak stresses exceed the yield strength but remain below the ultimate tensile strength. Moreover, these peaks are localized and not spread over large areas of the components, implying that the affected regions will undergo local plasticization without affecting the correct operation of the mechanical structure. The conductors and the aluminum shell are the most critical components of the magnet; their behavior is therefore analyzed in detail through figures and tables. Fig. 4 shows VM stress distribution across all phases of the analysis, while Table VI summarizes the peak stress values.

Another critical consideration for conductors is the gap that forms between them and the nearest external components. To address this, the gap and the contact pressures at the conductor–shoe interfaces were analyzed, with the objective of limiting peak gaps to approximately 10 μm. This objective has been fully achieved, and results are shown in Fig. 5 and Table VII.

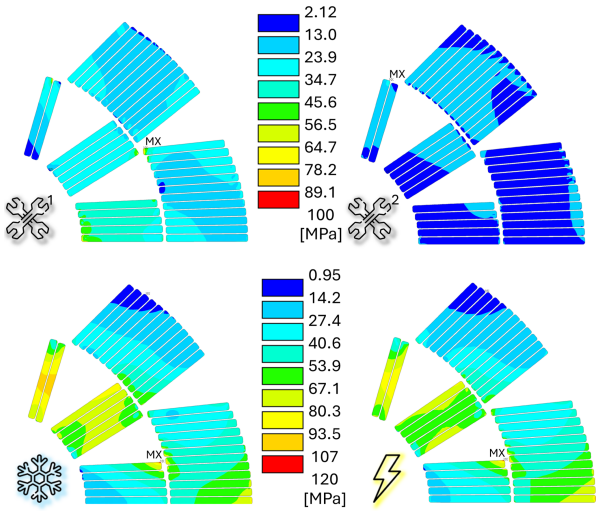

Fig. 4. VM stress distribution in conductors across all phases. The scale is set to the conductor yield strength at RT for the first two steps and at 1.9 K for the last two.

TABLE VI
PEAK STRESSES AND CORRESPONDING LIMITS (σ_{limit}) IN CONDUCTORS ACROSS THE MECHANICAL PHASES

	Step 1	Step 2	Step 3	Step 4
VM peak [MPa]	89	38	118	115
S1 peak [MPa]	38	8.6	30	30
S3 peak [MPa]	-100	-44	-115	-118
σ_{limit} [MPa]	100	100	120	120

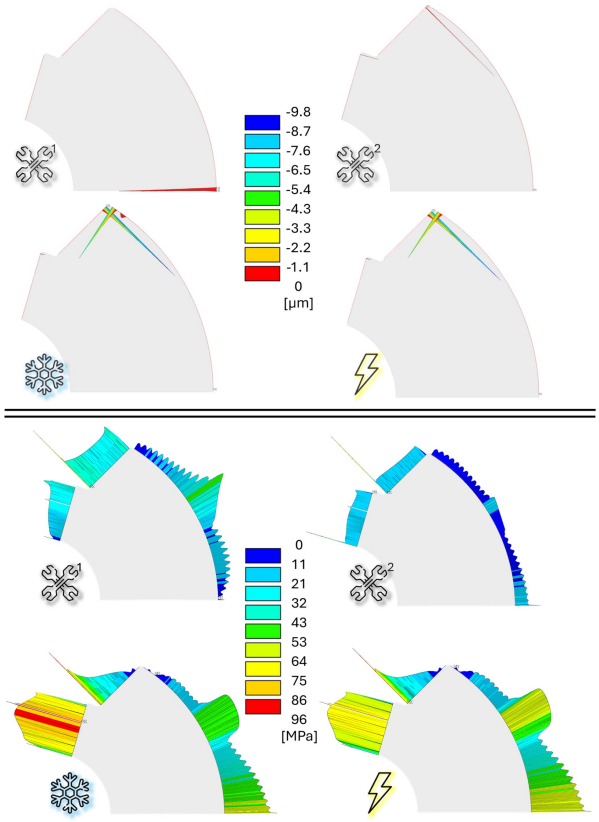

Fig. 5. Gap (on the top) and contact pressures (on the bottom) at the conductor–shoe interfaces across all steps.

TABLE VII
PEAK GAPS AND CONTACT PRESSURES AT CONDUCTOR–SHOE INTERFACES

	Step 1	Step 2	Step 3	Step 4
Gap max [μm]	0.4	0.1	9.8	9.2
Contact pressure peak [MPa]	79	52	96	87

TABLE VIII
PEAK STRESSES AND CORRESPONDING LIMITS (σ_{limit}) IN THE ALUMINUM SHELL ACROSS THE MECHANICAL PHASES

	Step 1	Step 2	Step 3	Step 4
VM peak [MPa]	132	37	163	163
σ_{limit} [MPa]	480	480	490	490

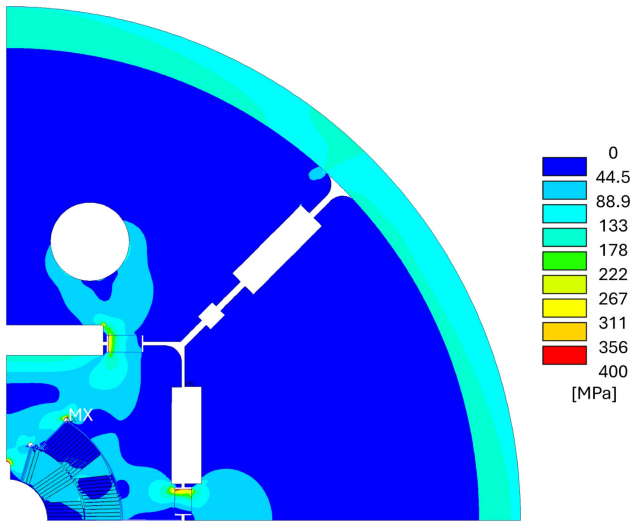

Fig. 6. Von Mises stress distribution, in the last step, over the full cross section of the magnet. The peak value of 400 MPa in the color scale was manually set to clarify the magnet's stress distribution.

As for the conductors, a detailed analysis was also carried out for the aluminum shell. Table VIII presents the VM stress values throughout all phases, demonstrating that they remain below the yield strength.

In conclusion, to provide an overall view of the magnet's mechanical behavior, Fig. 6 illustrates the VM stress distribution across the full quarter of the cross section at the end of the final analysis step.

V. CONCLUSION AND FUTURE DEVELOPMENTS

FEM analyses confirm that the current FalconD configuration withstands the expected loads, with mechanically acceptable stress levels ensuring proper operation across all phases. The gap analysis showed that the SS shoe provides effective support to the conductors through the contact surfaces, while the preliminary assembly study validated the feasibility of generating sufficient gaps for key insertion. Ongoing work focuses on optimizing winding parameters (at ASG) and refining the outer-layer coil head design (at INFN). In the coming months, a dummy copper coil will be wound at ASG and INFN will refine the assembly procedure to minimize stresses and avoid ovalization or fracture of the aluminum shell. Another objective is to finalize the 3D FEM analysis to define the design of the longitudinal preload system.

REFERENCES

[1] E. Todesco, "Status and perspectives of high field magnets for particle accelerators," *IEEE Trans. Appl. Supercond.*, vol. 35, no. 5, Aug. 2025, Art. no. 4003914, doi: 10.1109/TASC.2025.3558196.

[2] S. C. Hopkins, B. Medina-Clavijo, C. Barth, J. Fleiter, and A. Ballarino, "Design optimization, cabling and stability of large-diameter high J_c Nb_3Sn wires," *IEEE Trans. Appl. Supercond.*, vol. 33, no. 5, Aug. 2023, Art. no. 6000609, doi: 10.1109/TASC.2023.3254497.

[3] P. Ferracin et al., "Development of MQXF: The Nb_3Sn low-β quadrupole for the HiLumi LHC," *IEEE Trans. Appl. Supercond.*, vol. 26, no. 4, Jun. 2016, Art. no. 4000207, doi: 10.1109/TASC.2015.2510508.

[4] R. Valente et al., "Electromagnetic and mechanical study for the Nb_3Sn cosθ dipole model for the FCC," *IEEE Trans. Appl. Supercond.*, vol. 30, no. 4, Jun. 2020, Art. no. 4001905, doi: 10.1109/TASC.2020.2972219.

[5] A. Pampaloni et al., "Preliminary design of the Nb_3Sn cosθ short model for the FCC," *IEEE Trans. Appl. Supercond.*, vol. 31, no. 5, Aug. 2021, Art. no. 4900905, doi: 10.1109/TASC.2021.3061334.

[6] R. Valente et al., "Update on the electromagnetic design of the Nb_3Sn cosθ dipole model for FCC-hh," *IEEE Trans. Appl. Supercond.*, vol. 32, no. 4, Jun. 2022, Art. no. 4001005, doi: 10.1109/TASC.2023.3241832.

[7] R. Valente et al., "Optimization of electromagnetic design after winding tests for the Nb_3Sn cosθ dipole model for FCC-hh," *IEEE Trans. Appl. Supercond.*, vol. 33, no. 5, Aug. 2023, Art. no. 4601107, doi: 10.1109/TASC.2023.3246421.

[8] R. Valente et al., "Status on the development of the Nb_3Sn 12 t Falcon Dipole for the FCC-hh," *IEEE Trans. Appl. Supercond.*, vol. 34, no. 3, May 2024, Art. no. 4900405, doi: 10.1109/TASC.2023.3338166.

[9] A. Pampaloni et al., "Mechanical design of FalconD, a Nb_3Sn cosθ short model dipole for the FCC," *IEEE Trans. Appl. Supercond.*, vol. 32, no. 6, Sep. 2022, Art. no. 4000605, doi: 10.1109/TASC.2022.3149679.

[10] A. Pampaloni et al., "Updates on the mechanical design of FalconD, a Nb_3Sn cosθ short model dipole for FCC-hh," *IEEE Trans. Appl. Supercond.*, vol. 33, no. 5, Aug. 2023, Art. no. 4000805, doi: 10.1109/TASC.2023.3241832.

[11] S. Farinon et al., "Advancements in Nb_3Sn 12 T cosθ dipole development for next-generation accelerators: The INFN-CERN collaboration on the FalconD project," *IEEE Trans. Appl. Supercond.*, vol. 35, no. 5, Aug. 2025, Art. no. 4001905, doi: 10.1109/TASC.2024.3520944.

[12] S. Caspi et al., "The use of pressurized bladders for stress control of superconducting magnets," *IEEE Trans. Appl. Supercond.*, vol. 11, no. 1, pp. 2272–2275, Mar. 2001, doi: 10.1109/77.920313.

[13] G. Vallone, E. Anderssen, B. Bordini, and P. Ferracin, "A review of the mechanical properties of materials used in Nb_3Sn magnets for particle accelerators," *IEEE Trans. Appl. Supercond.*, vol. 33, no. 5, Aug. 2023, Art. no. 4002806, doi: 10.1109/TASC.2023.3248544.

[14] CERN, private communication.